Anchoring PdO$_x$ clusters on defective alumina for improved catalytic methane oxidation

Xiang Yu[1], Nina S. Genz [1,2], Rafael G. Mendes[3,4], Xinwei Ye[1], Florian Meirer [1], Maarten Nachtegaal [2], Matteo Monai [1]✉ & Bert M. Weckhuysen [1]✉

Evolution of the Pd active centers in size and spatial distribution leads to an irreversible deactivation in many high-temperature catalytic processes. This research demonstrates the use of a defective alumina (Al$_2$O$_{3-x}$) as catalyst support to anchor Pd atoms and suppress the growth of Pd clusters in catalytic methane oxidation. A combination of operando spectroscopy and density functional theory (DFT) calculations provide insights into the evolution of Pd species and reveals distinct catalytic methane oxidation mechanisms on Pd single atoms, clusters, and nanoparticles (NPs). Among these Pd species, the cluster active centers are found to be the most favorable participants in methane oxidation due to their high dispersion, high content of Pd^{2+} oxidation state, and resistance to deactivation by carbonates, bicarbonates, and water. The Pd/Al$_2$O$_{3-x}$ catalyst shows increased stability with respect to a Pd/Al$_2$O$_3$ counterpart during simulated aging in alternating reducing and oxidizing conditions due to stronger interactions with the support. This study demonstrates that defect engineering of non-reducible supports can constrain the evolution of active centers, which holds promising potential for widespread utilization across diverse industrial catalytic processes, including various hydrogenation and oxidation reactions.

Natural gas has been extensively used in power generation and other heating applications because of its abundant global storage, high knock resistance, and low carbon/hydrogen ratio[1–3]. However, methane (CH$_4$) has a climate forcing effect 87 times bigger than carbon dioxide (CO$_2$) over a 25-year period[4], and thus high specific activity is needed at low temperatures to avoid unwanted CH$_4$ emission, especially during engine start-up[5,6]. Hence, CH$_4$ catalytic oxidation is especially important in controlling harmful green-house gas emissions in exhaust after treatments of natural gas vehicles, which are emerging alternatives to gasoline[6–8]. Among the explored catalyst materials, Pd/Al$_2$O$_3$ is considered as the most desirable commercial catalyst for CH$_4$ oxidation under lean-burn conditions because of its high activity

and relatively low cost[6,8]. However, the gradual deactivation of Pd/Al$_2$O$_3$ catalysts over long periods of use remains a major problem for their practical implementation[3,8–10].

Previous studies have revealed many reasons for the deactivation of Pd/Al$_2$O$_3$ catalyst materials[3]. For instance, the active centers may be poisoned by SO$_x$, H$_2$O and carbonaceous species[11–14]. Such deactivation is non-permanent. Removal of surface poisons by adding periodic activation steps allow the catalyst to be regenerated or rejuvenated[15,16]. Permanent deactivation is typically due to the growth of Pd clusters into bigger Pd particles at high temperatures and during redox cycling, for which a practical solution has been rarely reported[7,10]. A practical way to suppress the nanoparticle growth is to modify the interaction

[1]Inorganic Chemistry and Catalysis, Debye Institute for Nanomaterials Science & Institute for Sustainable and Circular Chemistry, Utrecht University, Universiteitsweg 99, CG Utrecht 3584, The Netherlands. [2]Paul Scherrer Institute, Forschungsstrasse 111, Villigen 5232, Switzerland. [3]Soft Condensed Matter, Debye Institute for Nanomaterials Science, Utrecht University, Princetonplein 5, CC Utrecht 3584, The Netherlands. [4]Interfaces, Confinement, Matériaux et Nanostructures, CNRS-Orléans, 1b rue de la Férollerie, Orléans 45071, France. ✉e-mail: m.monai@uu.nl; b.m.weckhuysen@uu.nl

between support and metal species[17,18]. On the one hand, strong interactions secure the high dispersion degree of the active center that allows more metal atoms to participate in a reaction, while on the other hand the weak interactions lead to sintering and aggregation of metal NPs.

Although the conventional view suggests that only weak interactions exist between precious metals and alumina, a growing amount of experimental evidence has indicated that traces of so-called penta-coordinate aluminum (Al^V) appearing over γ-Al_2O_3 during thermal treatment can anchor precious metal ions[19]. However, due to the limited concentration of Al^V sites in γ-Al_2O_3, this interaction is mostly neglected in catalysis research. Of course, we should realize the distorted tetrahedral Al^{IV} sites, which are typically found in highly ordered alumina and silica-alumina, may also interfere with the identification of Al^V [20].

In this work, we have developed a synthetic route to increase the concentration of Al^V in amorphous alumina (Al_2O_{3-x}), having a high specific surface area and micro-mesoporous pore structure. Such support was used to anchor surface Pd species, preventing their aggregation and resulting in a more active and stable catalyst for CH_4 oxidation. High-angle annular dark-field scanning transmission electron microscopy (HAADF-STEM) and operando quick-extended X-ray absorption fine structure (QEXAFS) were used to study the evolution of Pd species on defective Al_2O_{3-x} and γ-Al_2O_3 supports during CH_4 oxidation. In order to reveal the relation between deactivation and the evolution of Pd species, the intrinsic activities and CH_4 catalytic oxidation mechanism over Pd nanoparticles (NPs), clusters and single-atom species present on Pd/Al_2O_3 and Pd/Al_2O_{3-x} were studied with the combination of operando Fourier transform infrared (FT-IR) spectroscopy and density functional theory (DFT) calculations.

Results and discussion

Evolution of Pd species over γ-Al_2O_3 and defective Al_2O_{3-x} during CH_4 oxidation

The synthesis of defective alumina was realized by pyrolysis of aluminum sulfate dissolved in a deep eutectic solvent composed of urea and thiourea (Fig. 1a, see Supplementary information, Section 1 for details). Pd/Al_2O_3 and Pd/Al_2O_{3-x} catalysts with a nominal Pd loading of 1 wt%, were prepared by the incipient wetness impregnation (IWI) method followed by calcination at 400 °C for 2 h (see Supplementary information, Sections 1.3 and 4 for details). The ^{27}Al solid-state nuclear magnetic resonance (ssNMR) results revealed the presence of three prominent peaks at around 5, 38 and 70 ppm over Al_2O_{3-x} (Fig. 1b), which can be ascribed to Al^{3+} species in tetrahedral (AlO_4 at 2–8 ppm), pentahedral (AlO_5 at 36–40 ppm) and octahedral (AlO_6 at 68-70 ppm) coordination, respectively[19,21]. To quantify the different Al species, the ^{27}Al ssNMR spectra were fitted by three components using a simple Czjzek model[22,23]. After loading of Pd, a decrease in the mole percent content of both Al^V (from 40 to 34%) and Al^{IV} (from 26 to 24%) on the Al_2O_{3-x} support was observed, accompanied by an elevation in the content of Al^{VI}. While previous research has evidenced the role of Al^V in the anchoring of isolated noble metals[19], the observed decrease in the relative content of Al^{IV} species here may also indicate binding of Pd atoms on Al^{IV}. One possible explanation is the occurrence of localized surface reconstruction caused by the interaction between distorted Al^{IV} species and Pd through oxygen bridging (Fig. 1a), leading to the conversion of tetrahedrally coordinated Al to an octahedral coordination structure. Furthermore, the total quantity of consumed Al^V and Al^{IV} sites was eight times greater than the amount of loaded Pd, which may be attributed to: (a) the fixation of Pd atoms requiring the consumption of multiple Al^V and Al^{IV} species[24] (Fig. 1a and Supplementary Information, Section 8.1 for details); (b) the introduction of Pd causing surface restructuring of amorphous alumina due to strong metal-support interaction[19,21]; and (c) the presence of trace amounts of water in the impregnation solution resulting in hydroxylation of Al^V and

distorted Al^{IV} sites. Notably, the remaining Al^V was still sufficient to immobilize an equal or even greater amount of Pd species or to restrict the mobility of Pd during the reaction[25]. In contrast, ^{27}Al NMR spectroscopy did not detect Al^V sites on γ-Al_2O_3 at room temperature, regardless of the presence of Pd species (Fig. 1c). The proportion between Al^{IV} and Al^{VI} also remained invariant on γ-Al_2O_3 before and after the loading process.

The catalytic activity of Pd/Al_2O_3 and Pd/Al_2O_{3-x} for the complete oxidation of CH_4 was evaluated using a fixed-bed downflow reactor. The light-off curves (Fig. 1d) for CH_4 conversion show that the fresh Pd/Al_2O_{3-x} exhibited higher catalytic activity (reaching 90% methane conversion at T_{90} = 367 °C) compared to Pd/Al_2O_3 (T_{90} = 429 °C). After ageing for 1.5 h at 500 °C with GHSV of 120,000 h^{-1}, Pd/Al_2O_{3-x}-aged lost some of its low-temperature activity, but the catalytic activity was improved at relatively high temperatures (Fig. 1d). In contrast, Pd/Al_2O_3-aged showed noticeably lower activity compared to Pd/Al_2O_3-fresh across all temperatures. The corresponding Arrhenius plots (Fig. 1e) demonstrated that Pd/Al_2O_3-aged possesses a higher apparent activation energy (125 kJ/mol) in comparison to Pd/Al_2O_3-fresh (72 kJ/mol), Pd/Al_2O_{3-x}-fresh (64 kJ/mol) and Pd/Al_2O_{3-x}-aged (66 kJ/mol). Based on the apparent activation energy values, it can be inferred that the active centers over Pd/Al_2O_{3-x} exhibit higher intrinsic activity than those on Pd/Al_2O_3, and that they undergo negligible changes in the aging process. On the other hand, the ageing process significantly changed the active centers of Pd/Al_2O_3, generating intrinsically less active Pd species. The intercepts of the fitted Arrhenius plots, in first approximation related to the quantity of active sites, provide additional evidence that fresh Pd/Al_2O_{3-x} possesses a higher quantity of accessible active centers than Pd/Al_2O_3, whereas ageing causes the loss of active species on both catalysts[26]. Furthermore, during stability testing at 500 °C, Pd/Al_2O_3 gradually deactivated over time, consistent with previous studies[10], while Pd/Al_2O_{3-x} remained relatively active for 15 h (Supplementary Information, Section 5 for details). Altogether, the results obtained suggest that Pd species on Al_2O_{3-x} were stabilized against thermally-induced deactivation processes during CH_4 oxidation.

We performed HAADF-STEM to obtain atomically resolved images of Pd species present on Pd/Al_2O_3 and Pd/Al_2O_{3-x}, for both fresh and aged catalysts. As shown in Fig. 1f, g, fresh Pd/Al_2O_3 consists mainly of small Pd NPs of 1–2 nm. After 1.5 h of ageing under reaction conditions, a fraction of the Pd species transformed into isolated Pd ions (Fig. 1j), potentially anchored on the generated Al^V sites during reaction[19]. Meanwhile the remaining Pd species sintered and agglomerated into large PdO NPs (Fig. 1h, i). In contrast, the Pd on the fresh Pd/Al_2O_{3-x} catalyst consisted mainly of Pd single-atom and low-nuclear PdO_x clusters (Fig. 1k). After ageing (Fig. 1l), a portion of the Pd species maintained their single-atom feature (Fig. 1m), while the other portion evolved into higher-nuclear Pd clusters (Fig. 1n), and no large NPs were observed (Supplementary Fig. 7), which we attribute to Pd anchoring to the more abundant Al^V sites on the defective alumina support.

In order to study the configuration of Pd species and their transformations during catalytic CH_4 oxidation, we employed operando QEXAFS with a time resolution of 1s[27–29]. The catalysts were heated in reaction conditions and subsequently tested at 500 °C for 1.5 h, allowing us to track alterations in the Pd structure and compare these with catalyst deactivation. The normalized Pd K-edge X-ray absorption near-edge spectroscopy (XANES) and Fourier transformed EXAFS binned at intervals of 5 s to enhance the signal-to-noise ratio, are shown in Fig. 2a, b. Pd was predominantly in an oxidized state under reaction conditions. As the white line and the first minimum of the XANES are sensitive to a change in structure and oxidation state of the metal species, we plotted the normalized X-ray absorption of the white line (denoted as A for Pd/Al_2O_3 and C for Pd/Al_2O_{3-x}) and the first minimum (denoted as B for Pd/Al_2O_3 and D for Pd/Al_2O_{3-x}) against time on stream (Fig. 2c). This allowed us to compare the subtle changes in
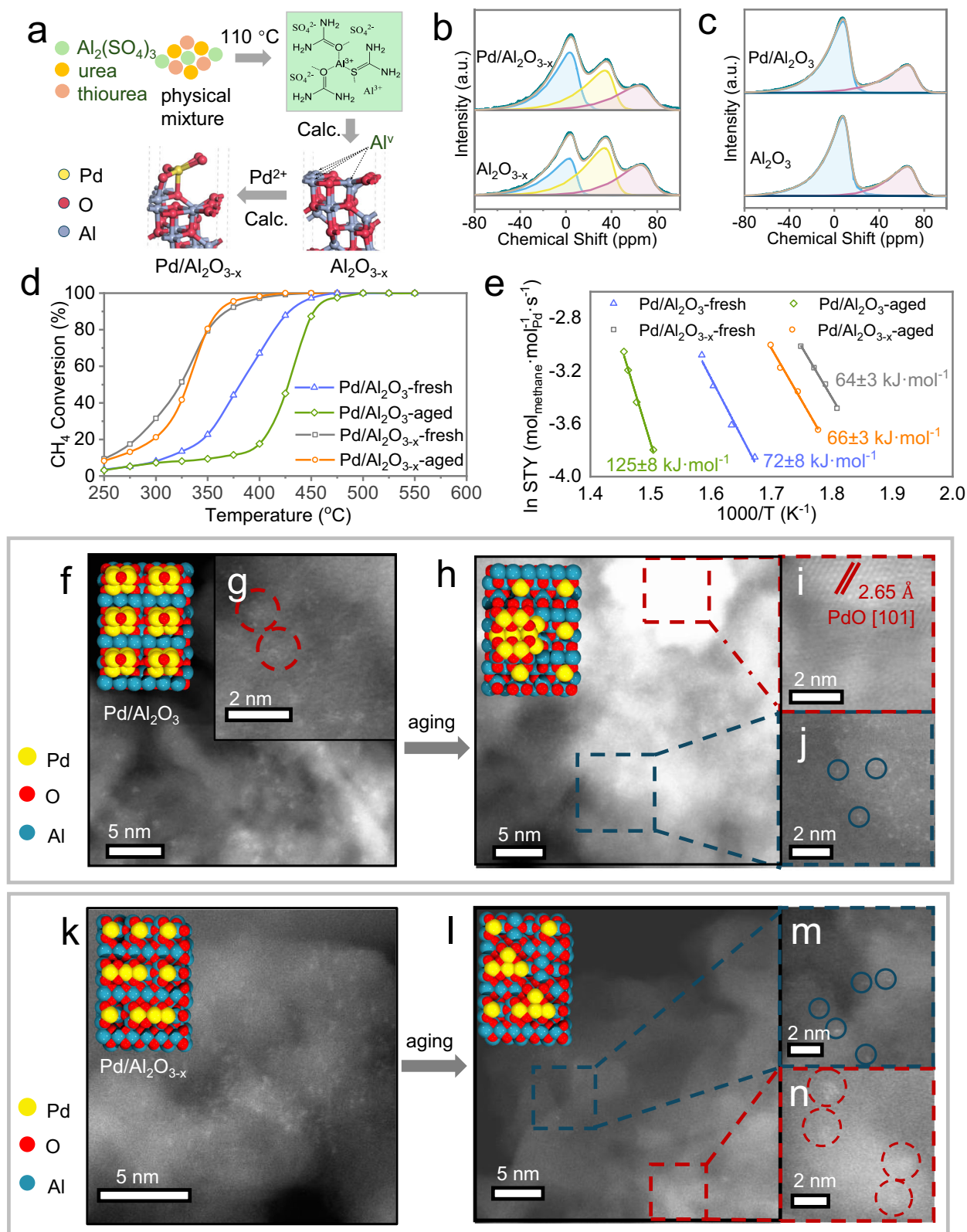
Fig. 1 | Stabilizing active palladium species on defective alumina sites.
a Schematic illustration of the synthesis of defective alumina (Al_2O_{3-x}) and Pd/Al_2O_{3-x}. ^{27}Al solid state nuclear magnetic resonance (ssNMR) spectra and respective fitting for Al_2O_{3-x} (**b** bottom), Pd/Al_2O_{3-x} (**b** top), γ-Al_2O_3 (**c** bottom) and Pd/Al_2O_3 (**c** top) The deconvoluted peaks, denoted by blue, yellow, and red colors, respectively represent the tetrahedral, pentahedral, and octahedral coordination Al species. **d** Light-off curves for catalytic methane (CH$_4$) oxidation over fresh and aged Pd/Al_2O_3 and Pd/Al_2O_{3-x} catalysts under reaction conditions (500 °C, 1.5 h).

Reaction conditions: CH$_4$:O$_2$:He = 2:8:90, 50 mg catalyst, GHSV = 60,000 h^{-1}.
e Arrhenius plots of the fresh and aged Pd catalysts. The high-angle annular dark-field scanning transmission electron microscopy (HAADF-STEM) images of Pd/Al_2O_3-fresh (**f**, **g**); Pd/Al_2O_3-aged (**h**–**j**); Pd/Al_2O_{3-x}-fresh (**k**) and Pd/Al_2O_{3-x}-aged (**l**–**n**). The red and blue dashed boxes represent respectively the regions where PdO$_x$ clusters/nanoparticles (NPs) and single atoms are present on the catalysts. Pd clusters are marked with the red rings, while Pd single atoms are marked with blue rings.
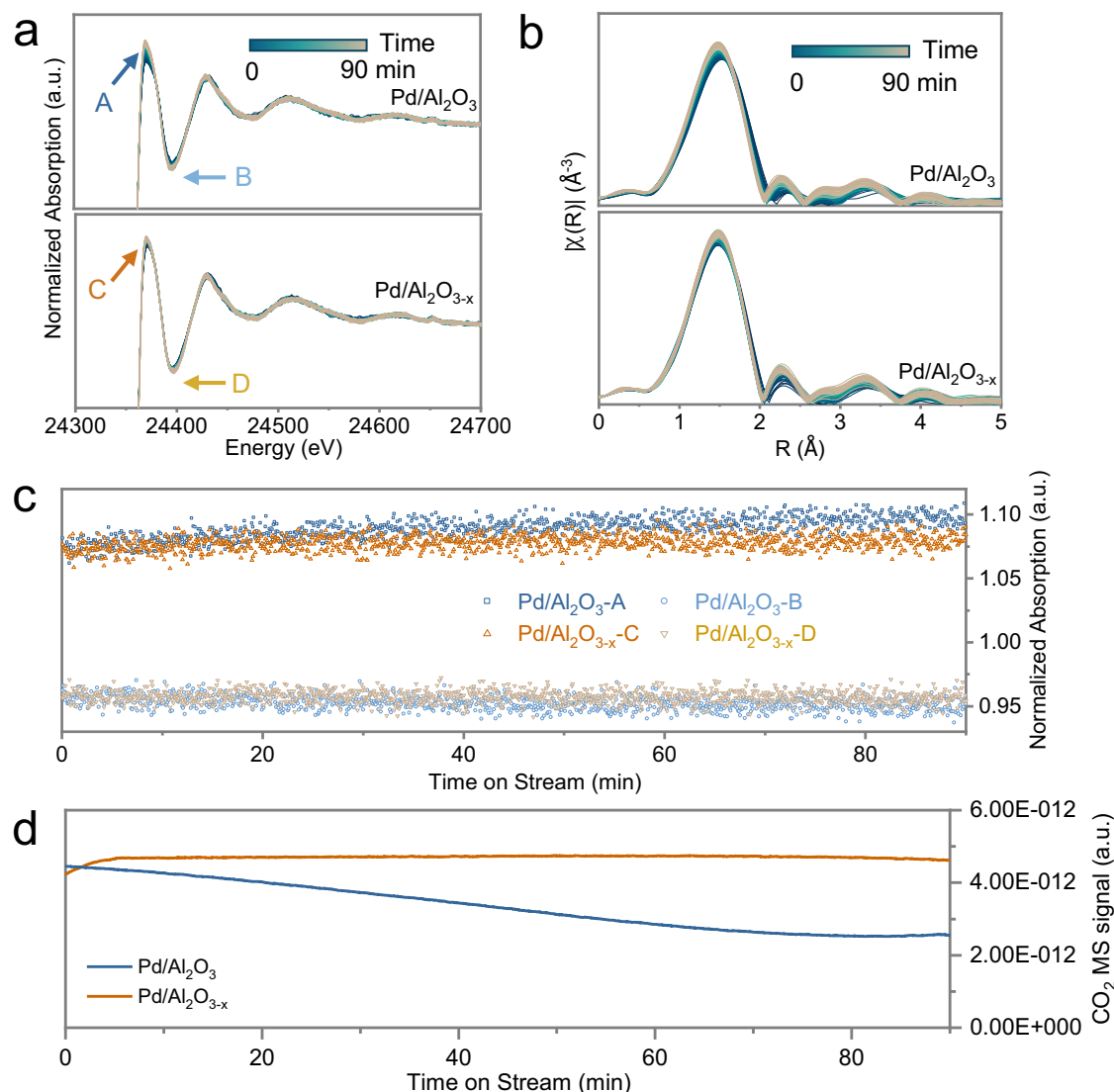
Fig. 2 | Correlation of Pd redox state and deactivation on different alumina supports. Operando X-ray absorption near-edge spectroscopy (XANES) (**a**) and R-space extended X-ray absorption fine structure (EXAFS) (**b**) of Pd/Al$_2$O$_3$ (top) and Pd/Al$_2$O$_{3-x}$ (bottom) with 5 s time resolution obtained during aging in reaction conditions (CH$_4$: O$_2$: He = 2:8:90, reaction temperature: 500 °C, and GHSV = 9,554 h^{-1}). **c** Plot of normalized X-ray absorption at the white line and first minimum (marked in Fig. 2a), as a function of time on stream. The corresponding on-line CO$_2$ mass spectrometry (MS) signal collected during the operando X-ray absorption spectroscopy (XAS) measurements (**d**).

oxidation states of Pd species during the aging process. The white line absorption values of Pd species in Pd/Al$_2$O$_{3-x}$ did not change appreciably, while for Pd/Al$_2$O$_3$ they increased slightly over time, suggesting a change in oxidation state of Pd species during the aging process. The R-space EXAFS indicated that the amount of metallic Pd species (at approximately 2.3 Å) on both catalysts remained roughly unchanged during this process (Fig. 2b), while the Pd-O contribution increased slightly. This can be attributed to growth of PdO NPs, consequently leading to an increase in Pd-O coordination number. It is worthwhile to mention that once steady state is reached under reaction conditions, the energies of the Pd K-edge absorption edge, the structures of the white line peak, and the absence of Pd-Pd scattering in the first shell of the EXAFS, all suggest the absence of metallic Pd as a composition of active centers. The on-line mass spectrometry (MS) results revealed a progressive decline in CO$_2$ production over Pd/Al$_2$O$_3$ in the aging process (Fig. 2d). Consistent with the catalytic test results, these findings suggest a correlation between deactivation and the subsequent oxidation or sintering of Pd species. In contrast, the defective

Al$_2$O$_{3-x}$ support significantly suppressed the sintering/deactivation of Pd.

Redox dynamics of Pd clusters and nanoparticles under CH$_4$/O$_2$ cycles

In typical three-way catalytic converters, the exhaust composition undergoes fast perturbations between reducing (also known as fuel-rich) and oxidizing (lean) conditions, close the stoichiometric point[30]. This is known to cause changes in Pd speciation and can cause rapid aging of the catalyst. To mimic such rapid changes in redox conditions and study their effect on Pd species and catalytic activity, we have performed operando QEXAFS with 1 s time-resolution during alternating pulses (i.e., modulation excitation, in short ME) of CH$_4$ and O$_2$. While the spectra were recorded, the products were measured by online MS at 2.5 s time resolution. (See Supplementary Information, Section 7.4 for details). Time-resolved Pd K-edge XANES of Pd/Al$_2$O$_3$ and Pd/Al$_2$O$_{3-x}$ at the white line region (24360–24400 eV) in a representative ME cycle are shown in Fig. 3a. Because Pd species are con-
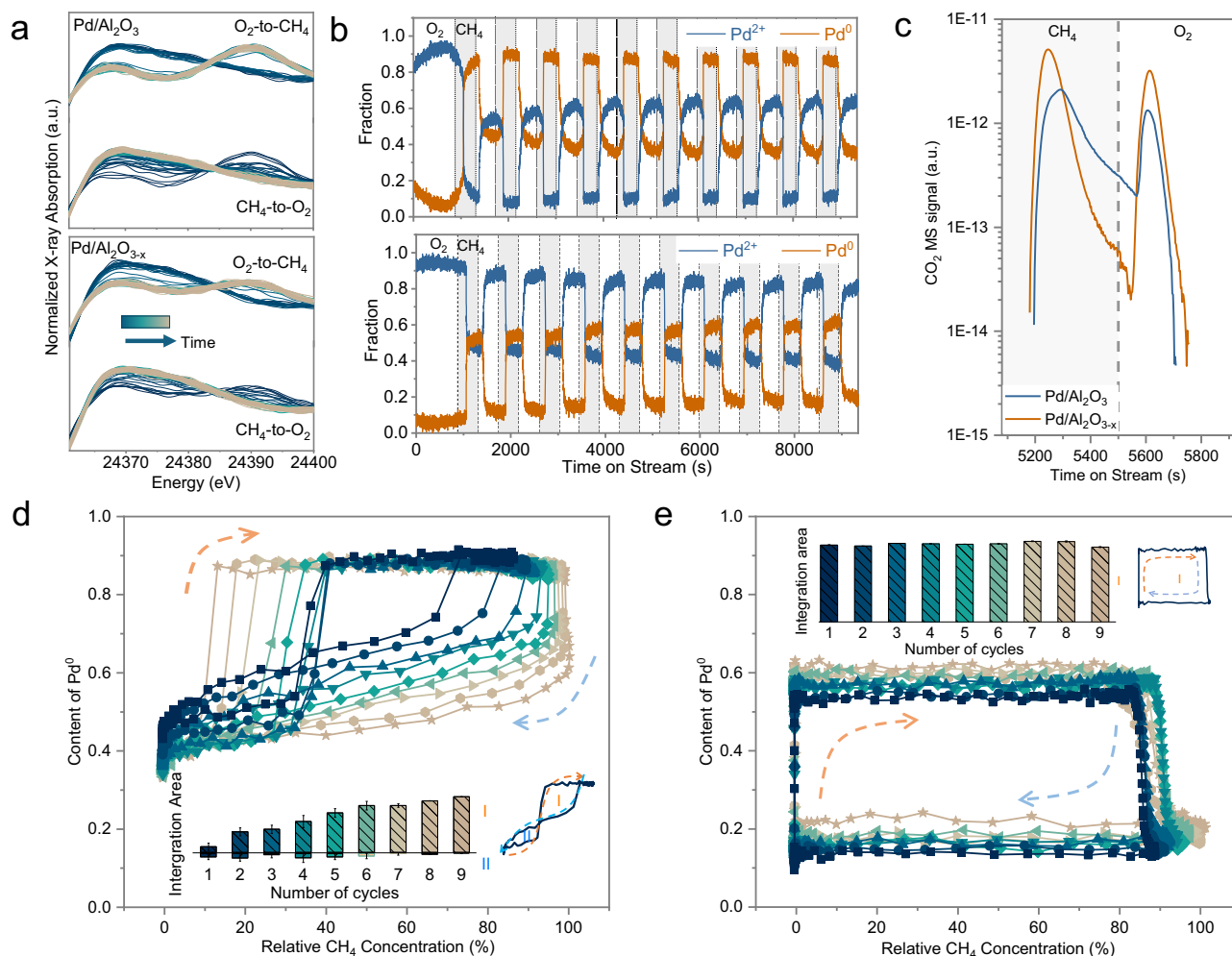
Fig. 3 | Redox dynamics of palladium species during simulated lean/rich cycles. a White line region of operando X-ray absorption near-edge spectroscopy (XANES) recorded at 1 s time resolution obtained upon switching between CH_4 and O_2. **b** Plots of Pd^{2+} and Pd^0 relative contents over Pd/Al_2O_3 (top) and Pd/Al_2O_3 (bottom) catalysts as a function of time, in the alternating CH_4/O_2 pulses. (Reaction temperature: 400 °C, and GHSV = 7,643 h^{-1}). **c** Plot of online CO_2 mass spectrometry (MS) signal as a function of time in a representative modulation excitation (ME) cycle. The variation in the content of Pd^0 species over Pd/Al_2O_3 (**d**) and Pd/Al_2O_3 (**e**) across the first to ninth reduction/oxidation cycles of the ME experiment, as a function of the relative CH_4/O_2 composition. The inserted bar chart illustrates the variation in the integrated area of the loops formed by the increase (during the reduction process) and decrease (during the oxidation process) of Pd^0 species in each oxidation/reduction cycle, as a function of the cycle number. Error bars indicate the 95% confidence interval.

sidered to follow the Mars-van Krevelen mechanism in CH_4 oxidation reactions, i.e., the lattice O in PdO may be taken away or replenished in redox reactions, the change in the absorption intensity of the white line can quantitatively describe the change in the average valence of the Pd species[8]. Thus, from the white line feature of the time-resolved XANES, we can infer that the valence of the Pd species on Pd/Al_2O_3 changed more significantly than that on Pd/Al_2O_3 in the ME cycle, and the Pd species on Pd/Al_2O_3 maintain a higher oxidation state in CH_4 atmosphere. In the ME experiments, the observed change in Pd species is mainly an interconversion between PdO and metallic Pd. To quantitatively characterize the changes in Pd oxidation state, we performed least squares linear combination fitting (LSLCF) of the Pd XANES, using PdO and metallic Pd as references. Considering that the XANES of atomically dispersed Pd species and PdO are very close (Supplementary Fig. 23), the fitted PdO fraction is the cumulative presence of single-atom Pd, PdO_x clusters and NPs. Hence, we designate these components as Pd^{2+}. The content of the Pd^{2+} and Pd^0 species as a function of time in the ME experiment are shown in Fig. 3b. Interestingly, in the initial switch from O_2 to CH_4 atmosphere on Pd/Al_2O_3, around 90% of the Pd species underwent a transformation from Pd^{2+} to Pd^0. However, in subsequent periodic pulsations alternating

between CH_4 and O_2, a proportion of approximately 40% Pd^0 and 10% Pd^{2+} was consistently maintained, while the remaining 50% of Pd species was oxidized or reduced depending on reaction atmosphere. The presence of irreducible Pd^{2+} species can be attributed to interfacial and single-atom Pd species, while Pd^0 species that cannot be oxidized may possibly arise from Pd atoms located within the interior of the NPs. These atoms are generated during the initial reduction process but remain metallic throughout the oxidation process probably due to the significant energy barrier associated with the diffusion of O atoms from the surface to the interior[31].

In the case of Pd/Al_2O_3, on the other hand, approximately 40% Pd^{2+} and 10% Pd^0 persisted unaffected by the oxidation/reduction atmosphere. This finding further suggests a higher proportion of interfacial/single-atom Pd species and smaller-sized PdO_x clusters/nanoparticles over Pd/Al_2O_3 compared to Pd/Al_2O_3. However, it is worth noting that the total quantity of Pd atoms capable of engaging in oxidation/reduction processes remained relatively similar between the two catalysts, accounting for approximately 50%. We propose that the remainder, non-redox-active species are located at the interface with alumina. Despite their comparable quantity, the redox-active Pd species on Pd/Al_2O_3 and Pd/Al_2O_3 can be anticipated to exhibit different

catalytic performance, because of their nature (more/less oxidic and dispersed).

Figure 3c illustrates the plots of the online CO_2 MS signal as a function of time in a representative ME cycle. Upon switching to a CH_4 atmosphere, the CO_2 signal on Pd/Al$_2$O$_3$-x exhibited an earlier onset and attained a higher peak compared to Pd/Al$_2$O$_3$. This potentially indicates a greater reducibility of PdO$_x$ clusters than NPs. Furthermore, on Pd/Al$_2$O$_3$-x there was a more pronounced decline in the CO_2 signal subsequent to reaching its peak in comparison with Pd/Al$_2$O$_3$. This observation may suggest either a lower CO_2 desorption energy on PdO$_x$ clusters, or a higher reduction energy barrier for the sub-surface Pd^{2+} on the PdO$_x$ NPs. The latter possibility can be ruled out as it does not align with the reduction rate of Pd^{2+} species indicated in Fig. 3b. Upon switching to the O_2 atmosphere, CO_2 MS signals were observed as well, albeit with an integrated area of approximately 30% compared to the previous process. The release of CO_2 at this stage was attributed to the oxidation of residual CH_4 from the previous gas pulse and/or to the oxidation of carbonaceous intermediates on the catalyst surface. The integration of CO_2 MS signals during reduction in CH_4 and oxidation in O_2 reveals that the amount of CO_2 produced on Pd/Al$_2$O$_3$-x is 1.45 and 2.92 times higher than on Pd/Al$_2$O$_3$, respectively. The potential reasons for the higher production of CO_2 on Pd/Al$_2$O$_3$-x can may include: (a) the PdO$_x$ clusters are more active than NPs to catalyze CH_4 oxidation; (b) the higher dispersion of PdO$_x$ clusters than NPs allows for the formation of a larger number of carbonaceous intermediates.

Considering gas mixing and reaction during alternating pulses of CH_4 and O_2, the ratio of Pd^0/Pd^{2+} species may exhibit dependence on the gas composition during the formed transients. Time-resolved QEXAFS and MS spectra can be combined in tracking the dependency of Pd species on the gaseous environment in the ME experiment. Since the combined content of Pd^{2+} and Pd^0, as determined from the unconstrained LCF results, adds up to 1 with less than 0.06 error, our focus is specifically on plotting the changes in the Pd^0 species content with respect to the relative concentrations of CH_4 and O_2 obtained from online MS, to gain a better understanding of the distinct responses of Pd atoms in clusters and NPs to the gas mixture interface during the reduction-oxidation cycles.

The reduction of Pd^{2+} on Pd/Al$_2$O$_3$ proceeded slowly at lower methane concentrations, necessitating a specific threshold of the CH_4/O_2 ratio in the environment to expedite the reduction process. Conversely, during the oxidation process, Pd^0 were oxidized upon the introduction of a small quantity of O_2, with the oxidation rate gradually diminishing over time. In a single reduction/oxidation cycle, the reduction and oxidation curves of the Pd species interlace. As depicted in Fig. 3d, we denoted the two intertwined loops formed by the variations in the Pd^0 species' content with respect to CH_4 concentration during the reduction-oxidation cycle as regions I and II. Region I is located at the higher relative CH_4 concentrations, while region II at the lower relative methane concentrations. A larger area in region I indicates that a greater number of Pd^{2+} species can be reduced at lower CH_4 concentrations, and more Pd^0 species can be oxidized at lower relative O_2 concentrations. Thus, the ratio of the areas I/II can serve as a descriptor of the reactivity of the Pd species. We integrated the areas of regions I and II in each ME cycle, and the changes in these integrated areas with cycle number are displayed in the inset of Fig. 3d. It is worth noting that the integrated area of region I increases with the number of cycles. This suggests that the ME cycling enhances the redox performance of Pd in Pd/Al$_2$O$_3$.

On the other hand, Pd in Pd/Al$_2$O$_3$-x exhibited different responses to the alternating reaction gas pulses in the ME experiment. Specifically, the reducible Pd^{2+} species underwent immediate and complete reduction to Pd^0 upon contact with CH_4. Similarly, during the oxidation process, the oxidizable Pd^0 species rapidly oxidize to Pd^{2+} upon exposure to O_2. Considering that the relative concentrations of CH_4

and O_2 were obtained from online MS, it can be inferred that once Pd species on Pd/Al$_2$O$_3$-x were subjected to alternating CH_4/O_2 pulses, they preferentially consumed all CH_4 or O_2 present in the gas mixture interface through the reduction/oxidation of Pd species, or the catalytic CH_4 oxidation. This process occurs at such a rapid rate that the apparent composition of Pd species appears to be independent of the relative concentrations of CH_4/O_2 in the gas mixture interface. Pd^0 content as a function of CH_4 concentration in the CH_4/O_2 pulse cycles forms a singular loop, region I in Fig. 3d, serving as a descriptor of the CH_4 oxidation reactivity. Notably, the integrated area of region III shows minimal sensitivity to the number of ME cycles. As discussed earlier, the reducible/oxidizable Pd species on Pd/Al$_2$O$_3$ and Pd/Al$_2$O$_3$-x originate from non-interface and non-core Pd atoms located on PdO$_x$ NPs and PdO$_x$ clusters, respectively. The above analysis of their responses to CH_4 and O_2 pulses suggests that Pd atoms within PdO$_x$ clusters exhibit higher catalytic reactivity towards CH_4 oxidation compared to PdO$_x$ NPs, with a lesser dependence on the relative concentration of CH_4 or O_2. With an increasing number of ME cycles, the activity of Pd atoms contained within PdO$_x$ NPs gradually improved, although it consistently remained lower than that of PdO$_x$ clusters. One possible explanation for this heightened activity is an increase in surface disorder or boundaries[31-33]. The gradual reduction in the amount of non-reducible Pd^{2+} species on Pd/Al$_2$O$_3$-x over time indicates the sintering of Pd in the ME experiment. However, the relatively stable area of region I of Fig. 3e implies that sintering does not significantly affect the activity of Pd atoms on the cluster surface.

Unraveling the reaction mechanism of CH_4 oxidation on Pd/Al$_2$O$_3$-x

Operando FT-IR spectroscopy was employed to further investigate the reaction mechanism of catalytic CH_4 oxidation. In all cases, the FT-IR spectra of the catalysts in a He atmosphere at 400 °C were subtracted (see Supplementary Information, Section 6.1 for details), to visualize the adsorbed organic intermediates. After the aged Pd/Al$_2$O$_3$ and Pd/Al$_2$O$_3$-x catalysts were subjected to reaction conditions (400 °C, CH_4:O_2: He = 2:4:90, GHSV = 60,000 h^{-1}) the FT-IR spectra were collected until reaching the steady states (Supplementary Information, Section 6.1 and Fig. 4a for details). The assignment of observed FT-IR absorption peaks to organic species is listed in Supplementary Table 6. A higher CH_4 absorption band at the wavenumber of 1305 cm^{-1} was observed on Pd/Al$_2$O$_3$ catalyst, because of the lower catalytic activity of this catalyst. Nevertheless, the gradual accumulation of formate, carbonate, and bicarbonate species on the surface of Pd/Al$_2$O$_3$ was observed. The accumulation of carbonates and bicarbonates as reaction products on Pd/Al$_2$O$_3$ implies that under reaction conditions, Pd species may be poisoned by these species, leading to reduced activity. This is consistent with the observation of a lower rate of CO_2 release over Pd/Al$_2$O$_3$ during ME (Fig. 3c). In contrast, when Pd/Al$_2$O$_3$-x is switched into the reaction atmosphere, the catalyst could maintain a relatively cleaner surface, with a certain amount of adsorbed bicarbonate and water, despite higher CH_4 conversion.

To record the build-up and degradation of the intermediates on the surface after excitation by different reactants, we performed operando FT-IR spectroscopy experiments with a time resolution of 1 min during alternating pulses of CH_4 and O_2 at 400 °C. The FT-IR spectra obtained over Pd/Al$_2$O$_3$ and Pd/Al$_2$O$_3$-x are shown in the Fig. 4b, c, respectively. To trace the occupation and exchange of different organic species with time, the FT-IR absorption peaks of all the observed species were integrated (Fig. 4d, e).

When switching from O_2 to CH_4 atmosphere, two intermediates, *CO and *HCOO, gradually accumulated on the surface of Pd/Al$_2$O$_3$ and Pd/Al$_2$O$_3$-x. The vibrational frequencies of the adsorbed CO on both catalysts are less than 2100 cm^{-1}, indicating that surface Pd species are metallic under these conditions[34,35], which agrees with the operando XAS results (Fig. 3b). Furthermore, it is interesting to note that *CO and
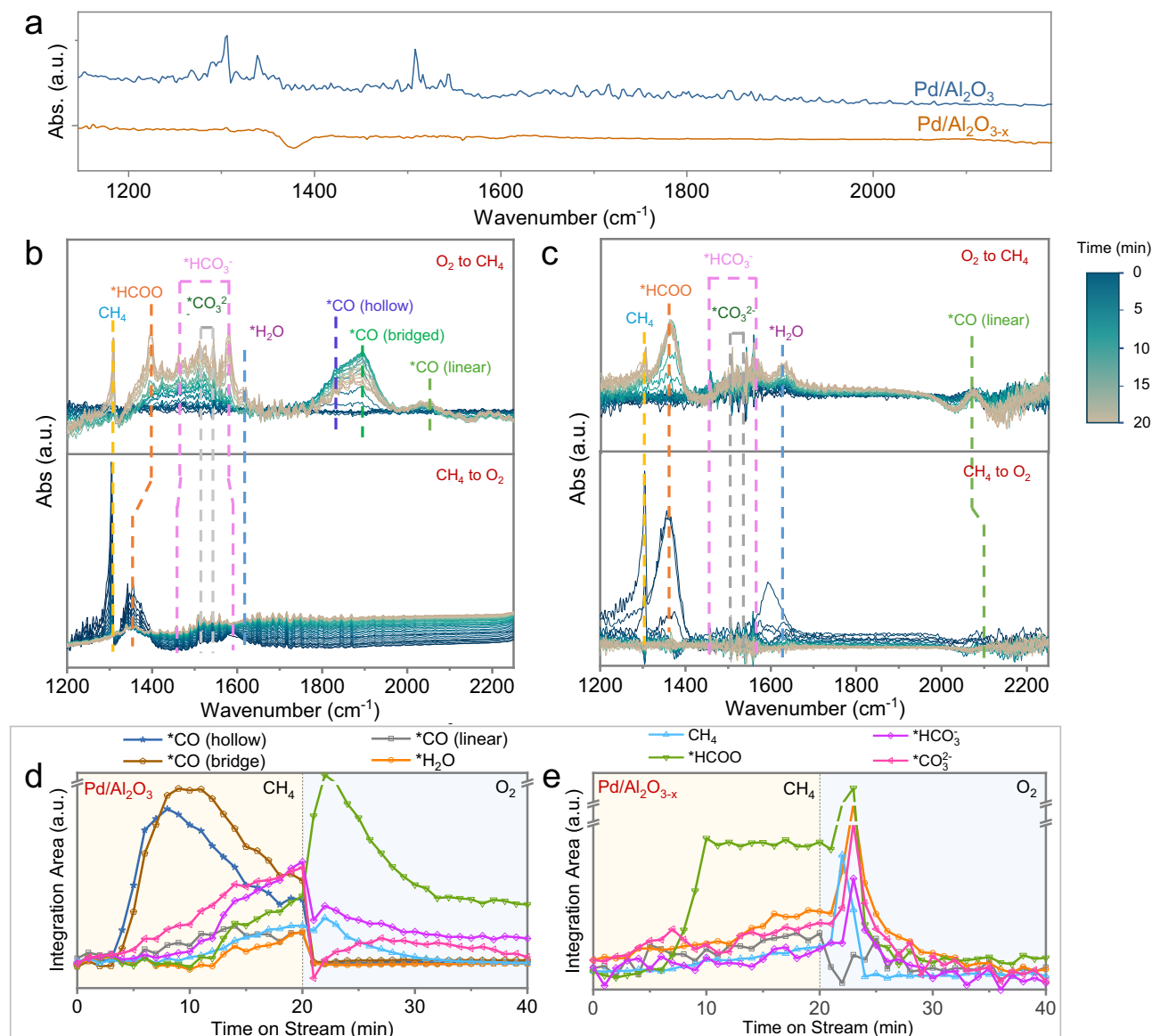
Fig. 4 | Surface chemistry of palladium clusters and nanoparticles during CH₄ oxidation. a Operando Fourier transform-infrared (FT-IR) spectra of Pd/Al₂O₃ (Pd NPs) and Pd/Al₂O₃₋ₓ (Pd clusters) at the steady states under reaction condition. CH₄ : O₂ : He = 2:8:90, reaction temperature = 400 °C, GHSV = 60,000 mL·g$_{cat}^{-1}$·h^{-1}.

In-situ FT-IR spectra of Pd/Al₂O₃ (**b**) and Pd/Al₂O₃₋ₓ (**c**) in the successive O₂-to-CH₄ and CH₄-to-O₂ switching processes, reaction temperature = 400 °C. Plots of the normalized integrated area of the IR absorption of each surface species on Pd/Al₂O₃ (**d**) and Pd/Al₂O₃₋ₓ (**e**) as a function of time during gas switching experiments.

*HCOO feature different adsorption modes on Pd/Al₂O₃ and Pd/Al₂O₃₋ₓ, because of their different surface structures. Specifically, the absence of infrared absorption peaks in the wavenumber range of 1800–2000 cm^{-1} (bridge- and hollow- CO absorption bands) on Pd/Al₂O₃₋ₓ suggest that the active centers of Pd/Al₂O₃₋ₓ are composed of single atoms and small clusters during reaction, because only in that case would geometrical effects prevent the bridge- or hollow-adsorption of CO[36]. Besides, the linearly adsorbed CO on Pd/Al₂O₃₋ₓ, exhibits a higher vibrational frequency than that on Pd/Al₂O₃, implying that the strong interaction between Pd and Al₂O₃₋ₓ affords the atomically dispersed Pd species a partial positive charge[37,38]. This is consistent with the observation that the C-H vibration of the adsorbed formate species exhibits a slightly lower frequency on Pd/Al₂O₃₋ₓ (1364 cm^{-1}) than on Pd/Al₂O₃ (1368 cm^{-1})[39,40]. From a time-dependence perspective (Fig. 3c), once switched from O₂ to CH₄ atmosphere, the hollow- and bridge-adsorbed CO covers the surface of Pd/Al₂O₃ preferentially amongst all intermediates. This can suggest the crucial role of the CO pathway on Pd/Al₂O₃. The coverage of the three CO

intermediates: hollow-, bridge- and linear-CO, begin to decrease at minutes 8, 11 and 14, respectively. This is either due to the desorption of CO caused by a competition with other adsorbates, or because the CO species are further oxidized by subsurface oxygen. Once the CO intermediates are formed, carbonates begin to accumulate on the surface of Pd/Al₂O₃. After ten minutes of CH₄ flow, when the coverage of carbonate reaches a specific threshold, the infrared absorption peaks for formate, bicarbonate and water become evident on Pd/Al₂O₃. Importantly, the accumulation of carbonate and bicarbonate on the surface of Pd NPs may induce alterations in the reaction pathways, favouring the formation of *HCOO. In contrast, although the *CO intermediate on Pd/Al₂O₃₋ₓ also appears early in the atmosphere of CH₄, its coverage remains relatively low. Interestingly, the coverage of *HCOO on Pd/Al₂O₃₋ₓ increases rapidly from 6 min onwards and became the dominant surface species.

On switching from CH₄ to O₂ atmosphere, *CO are immediately consumed on both Pd/Al₂O₃ and Pd/Al₂O₃₋ₓ, while the coverage of *HCOO increased abruptly. This may indicate that the oxidation of the
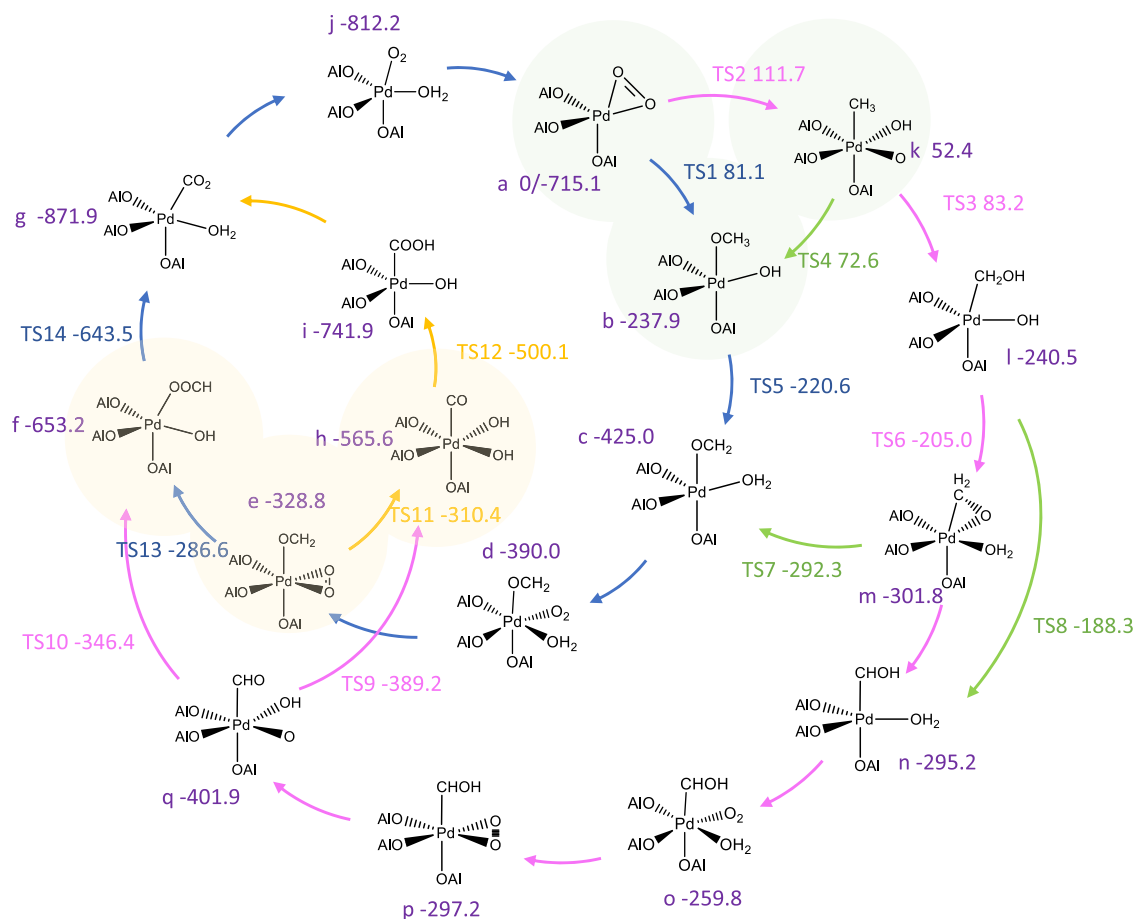
Fig. 5 | A model of CH$_4$ oxidation pathways on single-atom Pd. Reaction pathway network for CH$_4$ oxidation on single-atom Pd obtained from density functional theory (DFT) calculations (top). The values are the corresponding Gibbs free energies of the intermediates and transition states, in kJ/mol. The blue, yellow, pink, and green arrows respectively represent the formate branch of *OCH$_3$ pathway, the *CO branch of the *OCH$_3$ pathway, the *OCH$_2$ branch of the *CH$_3$ pathway, and the interconversions between these pathways. The green shaded region represents the elementary steps for CH$_4$ activation, leading to either *CH$_3$ or *OCH$_3$ pathways; while the yellow shaded region is the elemental steps where branching occurs between *CO and formate paths on the *OCH$_3$ pathway.

CO intermediate is kinetically more favorable. More importantly, from the degradation rates of *HCOO we can infer that Pd clusters or single atoms are significantly more active than Pd NPs in catalyzing the oxidation of formate intermediates. As the (OCO)$_s$ vibrational frequency of the adsorbed *HCOO is correlated with the oxidation states of the Pd species, it can be deduced that the Pd-O coordination number of the surface Pd over the clusters or single atoms is lower than that over PdO$_x$ NPs in the atmosphere of O$_2$, because Pd/Al$_2$O$_{3-x}$ exhibits a higher *HCOO vibrational frequency (1358 cm^{-1}) than Pd/Al$_2$O$_3$ (1349 cm^{-1}). This may account for the higher activity of Pd/Al$_2$O$_{3-x}$ towards *HCOO oxidation.

In the previous section, we proposed the hypothesis that Pd single-atoms may also participate in CH$_4$ oxidation without yielding Pd^0 species. That is, the Pd single atoms may accomplish a catalytic cycle through a combination of oxidative addition, reductive elimination, and transfer insertion, which is similar to the extensively reported catalytic mechanism of a homogeneous catalyst[41,42]. In light of the difficulty to corroborate this hypothesis experimentally, ab initio DFT calculations may afford us an insight into CH$_4$ oxidation pathways over the Pd single atoms.

In spite of the considerable theoretical effort being expended on the mechanism of the CH$_4$ oxidation over the specific facets of Pd or PdO, comparable work has rarely been done on the single-atom Pd species[32,43–49]. To implement this knowledge and examine our hypothesis, we have built a Pd$_1$/Al$_2$O$_3$ slab in which an isolated Pd atom was anchored on the (100) facet of γ-Al$_2$O$_3$ via O bridges[19]

(Supplementary Information, Section 8.1 for details). Referring to the individual CH$_4$ oxidation mechanisms postulated by previous studies, we proposed all CH$_4$ oxidation pathways over a single-atom Pd, and subsequently screened and optimized these pathways with DFT calculations. The proposed mechanism network is illustrated in Fig. 5, where a-j represent sketches of the structures of the catalyst (a) and different intermediates (b-j). The numbers following the letters are the calculated Gibbs free energies of the corresponding intermediates relative to the initial catalyst, at 400 °C. The arrows symbolize the conversion between individual intermediates, and TS1-14 refer to the transition states present in these conversion processes, whose relative Gibbs free energies are also indicated below. The configuration of the individual intermediates and transition state species is shown in Supplementary information, Sections 8.2 and 8.4. For comparison purposes, an energy profile of the entire reaction network was made (Fig. 6).

It is worth noting that the well-known carbide pathway is highly unlikely on the single-atom Pd, as the adsorption of carbene, carbyl and *C species on the single-atom Pd is thermodynamically unfavorable (Supplementary information, Section 8.2 for details). The activation of CH$_4$, highlighted in green shading in Fig. 5, is identified as a crucial rate-determining step in the overall CH$_4$ oxidation reaction. Compared to the *CH$_3$ pathway (marked by pink arrows), the *OCH$_x$ pathway (marked by blue arrows) is more favorable in terms of methane activation, as the *OCH$_x$ generation has a significantly lower activation energy than the *CH$_3$ production. The subsequent oxidation
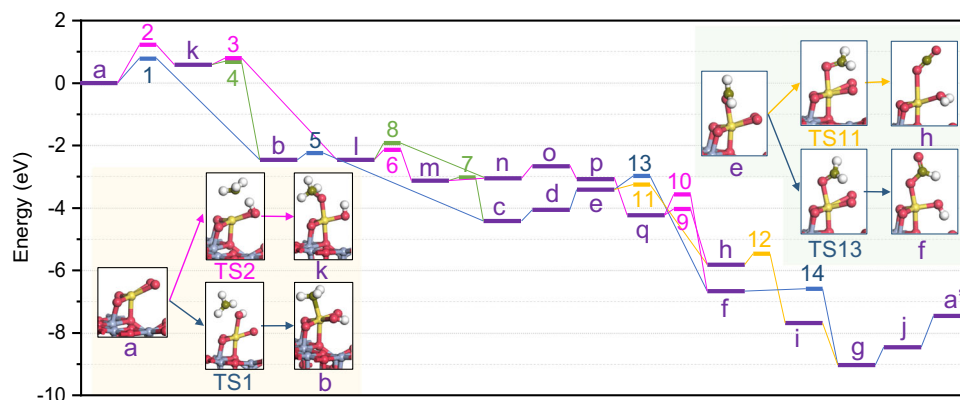
Fig. 6 | Gibbs free-energy profile of CH_4 oxidation on single-atom Pd. The letters and numbers annotated on the energy profile represent the intermediates and transition states along the various reaction pathways, corresponding to those depicted in Fig. 5. The green shaded region represents the elementary steps for CH_4 activation, leading to either $*CH_3$ or $*OCH_3$ pathways; while the yellow shaded region is the elemental steps where branching occurs between $*CO$ and formate paths on the $*OCH_3$ pathway.

of the carbonous intermediates all exhibits small energy barriers regardless of the pathways. The interconversions (marked by the green arrows) amongst the two pathways are all in favor of OCH_x pathways from the microkinetic perspective. These DFT results are corroborating the dominance of the OCH_x pathway in the catalytic mechanism.

According to the proposed model, the $*CO$ and $*HCOO$ intermediates observed in the operando FT-IR spectra may have originated from the oxidation of $*OCH_2$ by the coexistent active O (highlighted with yellow shadowing). Compared to $*CO$, the generation of $*HCOO$ is thermodynamically more favorable while kinetically unfavorable, but the energy barrier difference (23.8 kJ/mol) between these two intermediates is much smaller than the thermodynamic Gibbs free energy difference (87.6 kJ/mol). This may explain the preferential appearance of $*HCOO$ adsorbates. Notably, possibly because a reductive elimination leads to large changes in the valence of the single atom Pd, a high energy barrier for the desorption of water from the single-atom Pd was observed, which was higher than the activation energy of the CH_4 molecule. This is also consistent with the operando FT-IR spectroscopy results, implying that water can poison the single-atom Pd centers.

In comparison with the reaction pathways over a crystalline PdO surface unveiled by previous research[43], single-atom Pd manifests 20.3 kJ/mol higher CH_4 activation energy but lower energy barriers for further oxidation of carbon-containing intermediates. This explains the relatively cleaner surface of Pd/Al_2O_{3-x} under the reaction conditions as shown in the operando FT-IR spectra. The other rate-determining step to the single-atom Pd, the desorption of water, is less demanding for the crystalline PdO thermodynamically[43]. From a practical point of view, the low tolerance of Pd single atoms to water vapor, just as the poor resistance of PdO_x NPs to carbonates, may be detrimental to their activity, regardless of their high dispersion or intrinsic activity. These are conceivably important reasons for the growth of apparent activation energy during the deactivation of commercial Pd/Al_2O_3 catalysts and highlight the potential of Pd clusters as more stable active centers for CH_4 activation.

To sum up, a highly dispersed Pd catalyst was synthesized using defective Al_2O_{3-x} as a support and exhibited higher catalytic activity and stability in CH_4 oxidation compared to a counterpart Pd/Al_2O_3 catalyst. The evolution of the Pd active centers was significantly influenced by the type of support under the reaction conditions: the Pd clusters on γ-Al_2O_3 partially sintered and agglomerated into PdO_x nanoparticles (NPs), meanwhile being partially anchored as single atoms. In contrast, only a small fraction of the initial Pd single atoms in Pd/Al_2O_{3-x} were fused into clusters due to the constraint effect of Al^V species. The evolution of active centers under reaction conditions not only changes the quantity of Pd atoms available for participating in catalytic reaction, but also alters the intrinsic activities of the catalysts and their resistance to different poisoning species by changing the relative proportions of Pd NPs, clusters, and single atoms. The combined operando FT-IR spectroscopy, operando QEXAFS and DFT calculations revealed the mechanism of CH_4 oxidation reactions over Pd NPs, clusters and single atoms. The higher dispersion and lower adsorbate coverage of PdO_x clusters made them the most active in catalytic CH_4 oxidation. This paper showcases a method to ensure the abundance of Pd clusters by imposing restrictions on the evolution of Pd with defective alumina. We foresee that similar methods may be applied to other supports and metals, paving the way to more thermally stable and highly dispersed metal catalysts.

Methods

Catalyst synthesis
The Al_2O_{3-x} support was synthesized by calcining an eutectoid composed of urea (CON_2H_4, AR, Sigma-Aldrich), thiourea (CSN_2H_4, AR, Sigma-Aldrich) and aluminum sulfate octadecahydrate ($Al_2(SO_4)_3 \cdot 18H_2O$, AR, Sigma-Aldrich) in a tubular oven at 550 °C for 4 h. Parameters, such as feedstock types, feedstock ratio, calcination temperature and heat treatment time, were individually optimized to obtain the highest Al^V content, which are discussed in Supplementary information. The incorporation of 1 wt% of Pd onto γ-Al_2O_3 and Al_2O_{3-x} was approached by the incipient wetness impregnation (IWI) method, using palladium (II) chloride ($PdCl_2$, AR, Sigma-Aldrich) in methanol (AR, Sigma-Aldrich) as precursor, followed by heat treatment at 400 °C in air for 2 h (Supplementary information for further details).

Catalyst characterization
The crystalline structures, porous properties, morphology, and Al coordination structures of the support and catalysts were characterized using powder X-ray diffraction (XRD), gas physisorption measurements at 77 K, transmission electron microscopy (TEM), and solid-state ^{27}Al nuclear magnetic resonance spectroscopy (NMR), respectively. The presence of Pd were characterized by high-angle annular dark-field scanning transmission electron microscopy (HAADF-STEM) and Fourier transform infrared (FT-IR) spectroscopy of adsorbed CO. Full details are provided in the Supplementary information.

Catalyst testing
The catalysts were evaluated for CH_4 oxidation experiments in a quartz tube (inner diameter = 8 mm) reactor with a down flow over 75–212 μm catalyst particles, diluted by SiC crystals to make the catalyst bed volume up to 500 μL. The volume composition of the feed gas was 2

vol.% CH_4, 8 vol.% O_2 balanced with high purity helium. Stability tests and temperature-resolved activity tests were performed at gas hourly space velocities (GHSV) of 120,000 and 60,000 h^{-1}, respectively. On-line product analysis was performed with an Interscience custom-built Global Analyzer Solutions Compact GC4.0 gas chromatograph (GC). Blank experiments showed that reaction rates were negligible without catalyst.

Operando quick-XAS with on-line product analysis

Operando quick-X-ray absorption spectroscopy (Q-XAS) experiments with 1-s time resolution were performed at the SuperXAS beamline (X10DA) at the Swiss Light Source (SLS) in fluorescence mode. The X-ray beam from the 2.9 T bending magnet was collimated by a Pt coated mirror and monochromatized with a Si(111) channel-cut crystal Quick-XAS monochromator. The Si(111) crystal was rotated at a frequency of 1 Hz across the Pd K-edge, and the signals of the 20 cm long Ar/N_2 filled ionization chambers, a PIPS diode and the angular encoder were sampled at a frequency of 2 MHz. The edge energy for the Pd spectra was calibrated using a Pd foil in transmission mode, which was collected simultaneously with the quick-extended X-ray absorption fine structure (Q-EXAFS) spectra of the sample. The measurements were performed in a custom-built operando reaction cell (Supplementary information 7.1). Q-XAS data was subsequently evaluated using the ProQEXAFS software as well as self-developed Matlab™ code. Further information about the Q-XAS data processing can be found in the Supplementary information.

Operando FT-IR spectroscopy with on-line product analysis

Operando Fourier transform infrared (FT-IR) spectroscopy measurements with 1 min time resolution were carried out on a Bruker Tensor 37 FT-IR spectrometer equipped with a DTGS detector, to study the time-resolved formation and decomposition of the intermediates in CH_4 oxidation over different Pd species, under different reaction conditions. Product formation was followed by an Interscience custom-built Global Analyzer Solutions Compact GC4.0 gas chromatograph (GC). More experimental details, such as the design of the operando FT-IR cell, the preparation of the catalyst pellets, the experimental procedure and reaction conditions of the operando FT-IR spectroscopy measurements, and the data collection and processing methods can be found in the Supplementary information.

Density functional theory calculations

Ab initio density functional theory (DFT) calculations were performed using the Vienna Ab-initio Simulation Package (VASP)[50] with the projector-augmented wave (PAW) method[51,52]. The Perdew-Becke Ernzerhof (PBE) exchange-correlation functional was used[45]. The (100) facet of γ-Al_2O_3 obtained from Digne et al. was optimized and applied as the support[53,54], because the abundant Al^V sites on this facet[19]. A height of 15 Å in the z direction was used to separate the surface slab, in order to prevent interaction of intermediates. Isolated Pd atom was anchored to Al^V sites via oxygen bridges and the most stable position of Pd is tested on the Al_2O_3 (100) slab (see Supplementary information). All atoms were allowed to relax. The kinetic energy cutoff for the plane wave basis set was 500 eV. The Monkhorst-Pack mesh k-points of $(5 \times 3 \times 1)$ for Pd_1/Al_2O_3 and Al_2O_3 slab were used to sample the surface Brillouin zone to assure accuracy. Structural optimization was performed by use of the conjugate gradient method, the geometries were converged to 10^{-4} eV and electronic convergence was set at 10^{-5} eV. For the gas-phase calculations, the CH_4, CO_2, O_2, and H_2O molecules were placed at the center of a $10 \times 10 \times 10$ Å unit cell, with only a G cantered grid for k-point sampling. A width of 0.00002 eV was applied for electron smearing. The reaction pathways discussed in the main text have been calculated by the nudged elastic band (NEB) approach as implemented in VASP[54,55]. To confirm that all transition geometries were in a first-order saddle point on the potential energy surface, the frequency analysis was performed. The Hessian matrix was constructed using a finite displacement approach with a step size of 0.02 Å for displacement of individual atoms along each Cartesian coordinate. These frequencies were used to determine the zero-point energy (ZPE) correction to the energy of the geometries of the initial, transition, and final states.

Data availability

All data utilized in the manuscript have been uploaded to the YODA repository and are available under https://science.yoda.uu.nl/research/browse?dir=%2Fresearch-published-papers%2FYu%2C%20X_NatureCommunications_2024.

References

1. Zarur, A. J. & Ying, J. Y. Reverse microemulsion synthesis of nanostructured complex oxides for catalytic combustion. *Nature* **403**, 65–67 (2000).
2. Choudhary, T., Banerjee, S. & Choudhary, V. Catalysts for combustion of methane and lower alkanes. *Appl. Catal. A Gen.* **234**, 1–23 (2002).
3. Gélin, P. & Primet, M. Complete oxidation of methane at low temperature over noble metal-based catalysts: a review. *Appl. Catal. B Environ.* **39**, 1–37 (2002).
4. Balcombe, P., Speirs, J. F., Brandon, N. P. & Hawkes, A. D. Methane emissions: choosing the right climate metric and time horizon. *Environ. Sci. Process. Impacts* **20**, 1323–1339 (2018).
5. Hutter, R., De Libero, L., Elbert, P. & Onder, C. H. Catalytic methane oxidation in the exhaust gas after treatment of a lean-burn natural gas engine. *Chem. Eng. J.* **349**, 156–167 (2018).
6. He, L., Fan, Y., Bellettre, J., Yue, J. & Luo, L. A review on catalytic methane combustion at low temperatures: Catalysts, mechanisms, reaction conditions and reactor designs. *Renew. Sustain. Energy Rev.* **119**, 109589 (2020).
7. Cargnello, M. et al. Exceptional activity for methane combustion over modular Pd@CeO$_2$ subunits on functionalized Al$_2$O$_3$. *Science* **337**, 713–717 (2012).
8. Ciuparu, D., Lyubovsky, M. R., Altman, E., Pfefferle, L. D. & Datye, A. Catalytic combustion of methane over palladium-based catalysts. *Catal. Rev.* **44**, 593–649 (2002).
9. Monai, M., Montini, T., Gorte, R. J. & Fornasiero, P. Catalytic oxidation of methane: Pd and beyond. *Eur. J. Inorg. Chem.* **2018**, 2884–2893 (2018).
10. Euzen, P., Le Gal, J.-H., Rebours, B. & Martin, G. Deactivation of palladium catalyst in catalytic combustion of methane. *Catal. Today* **47**, 19–27 (1999).
11. Ciuparu, D., Katsikis, N. & Pfefferle, L. Temperature and time dependence of the water inhibition effect on supported palladium catalyst for methane combustion. *Appl. Catal. A Gen.* **216**, 209–215 (2001).
12. Monai, M. et al. The effect of sulfur dioxide on the activity of hierarchical Pd-based catalysts in methane combustion. *Appl. Catal. B Environ.* **202**, 72–83 (2017).
13. Escandón, L. S., Ordóñez, S., Vega, A. & Díez, F. V. Sulphur poisoning of palladium catalysts used for methane combustion: effect of the support. *J. Hazard. Mater.* **153**, 742–750 (2008).
14. Gelin, P., Urfels, L., Primet, M. & Tena, E. Complete oxidation of methane at low temperature over Pt and Pd catalysts for the abatement of lean-burn natural gas fuelled vehicles emissions: influence of water and sulphur containing compounds. *Catal. Today* **83**, 45–57 (2003).
15. Gremminger, A. et al. Sulfur poisoning and regeneration of bimetallic Pd-Pt methane oxidation catalysts. *Appl. Catal. B Environ.* **218**, 833–843 (2017).
16. Honkanen, M. et al. Regeneration of sulfur-poisoned Pd-based catalyst for natural gas oxidation. *J. Catal.* **358**, 253–265 (2018).

17. Haller, G. L. & Resasco, D. E. Metal–support interaction: group VIII metals and reducible oxides. *Adv. Catal.* **36**, 173–235 (1989).

18. Jones, J. et al. Thermally stable single-atom platinum-on-ceria catalysts via atom trapping. *Science* **353**, 150–154 (2016).

19. Kwak, J. H. et al. Coordinatively unsaturated Al^{3+} centers as binding sites for active catalyst phases of platinum on γ-Al_2O_3. *Science* **325**, 1670–1673 (2009).

20. Chen, K., Gan, Z., Horstmeier, S. & White, J. L. Distribution of aluminum species in zeolite catalysts: ^{27}Al NMR of framework, partially-coordinated framework, and non-framework moieties. *J. Am. Chem. Soc.* **143**, 6669–6680 (2021).

21. Gutierrez, G. & Johansson, B. Molecular dynamics study of structural properties of amorphous Al_2O_3. *Phys. Rev. B* **65**, 104202 (2002).

22. de Lacaillerie, J.-Bd. E., Fretigny, C., Massiot, D. & NMR, M. A. S. spectra of quadrupolar nuclei in disordered solids: the Czjzek model. *J. Magn. Reson.* **192**, 244–251 (2008).

23. Massiot, D. et al. Modelling one-and two-dimensional solid-state NMR spectra. *Magn. Reson. Chem.* **40**, 70–76 (2002).

24. Dessal, C. et al. Atmosphere-dependent stability and mobility of catalytic Pt single atoms and clusters on γ-Al_2O_3. *Nanoscale* **11**, 6897–6904 (2019).

25. Shi, L. et al. Al_2O_3 nanosheets rich in pentacoordinate Al^{3+} ions stabilize Pt-Sn clusters for propane dehydrogenation. *Angew. Chem. Int. Ed.* **54**, 13994–13998 (2015).

26. Zhdanov, V. P. Arrhenius parameters for rate processes on solid surfaces. *Surf. Sci. Rep.* **12**, 185–242 (1991).

27. Vogt, C. et al. Unravelling structure sensitivity in CO_2 hydrogenation over nickel. *Nat. Catalysis* **1**, 127–134 (2018).

28. Petousis, I. et al. High-throughput screening of inorganic compounds for the discovery of novel dielectric and optical materials. *Sci. Data* **4**, 1–12 (2017).

29. Finzel, J. et al. Limits of detection for EXAFS characterization of heterogeneous single-atom catalysts. *ACS Catal.* **13**, 6462–6473 (2023).

30. Fujiwara, A. et al. Surface state changes of Pd three-way catalysts under dynamic lean/rich perturbation compared with static condition. *J. Phys. Chem. C.* **127**, 279–288 (2022).

31. Atkinson, A. Transport processes during the growth of oxide films at elevated temperature. *Rev. Mod. Phys.* **57**, 437–470 (1985).

32. Bunting, R. J., Cheng, X., Thompson, J. & Hu, P. Amorphous surface PdO_X and its activity toward methane combustion. *ACS Catal.* **9**, 10317–10323 (2019).

33. Huang, W. et al. Steam-created grain boundaries for methane C–H activation in palladium catalysts. *Science* **373**, 1518–1523 (2021).

34. Xu, X., Chen, P. & Goodman, D. W. A comparative study of the coadsorption of carbon monoxide and nitric oxide on Pd (100), Pd (111), and silica-supported palladium particles with infrared reflection-absorption spectroscopy. *J. Phys. Chem.* **98**, 9242–9246 (1994).

35. Jang, E. J., Lee, J., Oh, D. G. & Kwak, J. H. CH_4 oxidation activity in Pd and Pt–Pd bimetallic catalysts: correlation with surface PdOx quantified from the DRIFTS study. *ACS Catal.* **11**, 5894–5905 (2021).

36. Zhang, L. et al. Efficient and durable Au alloyed Pd single-atom catalyst for the Ullmann reaction of aryl chlorides in water. *ACS Catal.* **4**, 1546–1553 (2014).

37. Ma, L., Chen, X., Li, J., Chang, H. & Schwank, J. W. Electronic metal-support interactions in Pt/FeOx nanospheres for CO oxidation. *Catal. Today* **355**, 539–546 (2020).

38. Wei, T., Wang, J. & Goodman, D. W. Characterization and chemical properties of Pd– Au alloy surfaces. *J. Phys. Chem. C* **111**, 8781–8788 (2007).

39. Vasileff, A. et al. Selectivity control for electrochemical CO_2 reduction by charge redistribution on the surface of copper alloys. *ACS Catal.* **9**, 9411–9417 (2019).

40. Li, C., Domen, K., Maruya, K. I. & Onishi, T. Spectroscopic identification of adsorbed species derived from adsorption and decomposition of formic acid, methanol, and formaldehyde on cerium oxide. *J. Catal.* **125**, 445–455 (1990).

41. Hill, C. L. & Prosser-McCartha, C. M. Homogeneous catalysis by transition metal oxygen anion clusters. *Coord. Chem. Rev.* **143**, 407–455 (1995).

42. Westbrook, C. K. Chemical kinetics of hydrocarbon ignition in practical combustion systems. *Proc. Combust. Inst.* **28**, 1563–1577 (2000).

43. Stotz, H. et al. Surface reaction kinetics of methane oxidation over PdO. *J. Catal.* **370**, 152–175 (2019).

44. Trinchero, A., Hellman, A. & Grönbeck, H. Methane oxidation over Pd and Pt studied by DFT and kinetic modeling. *Surf. Sci.* **616**, 206–213 (2013).

45. Antony, A., Asthagiri, A. & Weaver, J. F. Pathways and kinetics of methane and ethane C–H bond cleavage on PdO. *J. Chem. Phys.* **139**, 104702 (2013).

46. Dianat, A., Seriani, N., Ciacchi, L. C., Bobeth, M. & Cuniberti, G. DFT study of reaction processes of methane combustion on PdO (1 0 0). *Chem. Phys.* **443**, 53–60 (2014).

47. Xu, J. et al. Single-atom Rh on high-index CeO_2 facet for highly enhanced catalytic CO oxidation. *Angew. Chem. Int. Ed.* **62**, e202302877 (2023).

48. Chen, L., Wu, X.-P. & Gong, X.-Q. Unique catalytic mechanisms of methanol dehydrogenation at Pd-doped ceria: A DFT+ U study. *J. Chem. Phys.* **156**, 134701 (2022).

49. Kim, Y. et al. Surface density dependent catalytic activity of single palladium atoms supported on ceria. *Angew. Chem. Int. Ed.* **60**, 23028–23028 (2021).

50. Kresse, G. & Furthmüller, J. Efficient iterative schemes for ab initio total-energy calculations using a plane-wave basis set. *Phys. Rev. B* **54**, 11169 (1996).

51. Grimme, S. Semiempirical GGA-type density functional constructed with a long-range dispersion correction. *J. Comput. Chem.* **27**, 1787–1799 (2006).

52. Kresse, G. & Furthmüller, J. Efficiency of ab-initio total energy calculations for metals and semiconductors using a plane-wave basis set. *Comput. Mater. Sci.* **6**, 15–50 (1996).

53. Digne, M., Sautet, P., Raybaud, P., Euzen, P. & Toulhoat, H. Use of DFT to achieve a rational understanding of acid–basic properties of γ-alumina surfaces. *J. Catal.* **226**, 54–68 (2004).

54. Perdew, J. P., Burke, K. & Ernzerhof, M. Generalized gradient approximation made simple. *Phys. Rev. Lett.* **77**, 3865 (1996).

55. Sheppard, D., Xiao, P., Chemelewski, W., Johnson, D. D. & Henkelman, G. A generalized solid-state nudged elastic band method. *J. Chem. Phys.* **136**, 074103 (2012).

Acknowledgements

Author contributions

X.Yu designed and performed most of the experiments and theoretical calculations, processed the acquired data, and drafted the manuscript. N.S.G. and X.Ye performed part of the experiments. R.M. performed the STEM imaging. M.M., F.M., M.H. and M.N. participated in the discussion

of the results. B.M.W. and M.M. supervised the research and the preparation and writing of the different versions of the article.

Competing interests

The authors declare no competing interests.

Additional information

Supplementary information The online version contains supplementary material available at https://doi.org/10.1038/s41467-024-50216-0.

Correspondence and requests for materials should be addressed to Matteo Monai or Bert M. Weckhuysen.

Peer review information *Nature Communications* thanks the anonymous reviewers for their contribution to the peer review of this work. A peer review file is available.

Reprints and permissions information is available at http://www.nature.com/reprints

Publisher's note Springer Nature remains neutral with regard to jurisdictional claims in published maps and institutional affiliations.